Applied Catalysis B: Environmental 165 (2015) 676–686

Contents lists available at ScienceDirect

Applied Catalysis B: Environmental

journal homepage: www.elsevier.com/locate/apcatb

Electrochemical oxidation of CO and methanol on Pt–Ru catalysts supported on carbon nanofibers: the influence of synthesis method

J.C. Calderón[a], G. García[a], L. Calvillo[b,1], J.L. Rodríguez[a], M.J. Lázaro[b], E. Pastor[a,*]

[a] Dpto. Química-Física, Instituto de Materiales y Nanotecnología, Universidad de La Laguna, Avda. Astrofísico Francisco Sánchez s/n, 38071, La Laguna (Tenerife), Spain
[b] Instituto de Carboquímica (CSIC), Miguel Luesma Castán 4, 50018, Zaragoza, Spain

ARTICLE INFO

Article history:
Received 29 August 2014
Received in revised form 21 October 2014
Accepted 29 October 2014
Available online 3 November 2014

Keywords:
Pt–Ru catalysts
Carbon nanofibers
Synthesis methods
Carbon monoxide
Methanol electrooxidation.

ABSTRACT

Pt–Ru catalysts supported on carbon nanofibers were synthesized by different synthesis methods: reduction with sodium borohydride, methanol and formate ions (denoted as BM, MeOH and SFM, respectively). The catalyst synthesized by the SFM route was heat-treated (denoted as SFM TT) in order to enhance its catalytic activity, generating in this way a new catalyst. Physical characterization was performed by means of energy-dispersive X-ray (EDX), X-ray diffraction (XRD), X-ray photoelectron spectroscopy (XPS) and transmission electron microscopy (TEM). Results showed that Pt–Ru/CNF catalysts with similar metal content (20 wt%) and atomic ratio (Pt:Ru 1:1) can be obtained by all methodologies. In order to determine the CO tolerance and the electroactive areas of the materials, adsorbed CO stripping experiments were performed. CO stripping curves were modified with the addition of Ru that shifts the onset and peak electrooxidation potentials to more negative values compared with those obtained for the Pt/C catalyst. SFM TT catalyst delivered the highest current densities during the methanol oxidation reaction. Materials synthesized by SFM and MeOH procedures also exhibited high current densities, whereas the samples obtained by the BM method presented the lowest activity, similar to that for the commercial Pt–Ru/C catalyst from E-TEK. Differential electrochemical mass spectrometry (DEMS) was applied to determine the onset potential for the both electrooxidation reactions as well as the energy conversion efficiency for methanol oxidation to CO_2. It is remarkable that the material prepared by the SFM TT route delivered the highest current density during the methanol oxidation reaction and also provided the lowest conversion efficiency to CO_2.

© 2014 Elsevier B.V. All rights reserved.

1. Introduction

Platinum-transition metal alloys as catalyst for fuel cell (FC) anodes become of paramount importance due to the requirement of reducing the production cost of FC components with an increment of its performance. Different Pt-based alloys like Pt–Sn [1], Pt–Re [2] and Pt–Mo [3,4] have been studied as catalyst for alcohol electrooxidation. In this context, Pt–Ru nanoparticles (NPs) supported on different carbon substrates have shown to be one of the best materials for the methanol electrooxidation reaction [5,6]. It is well known that the introduction of Ru in Pt-based catalysts promotes the oxidation of CO, which is produced as intermediate during the methanol oxidation reaction [7,8]. The last effect has been attributed to the fact that Ru forms oxygenated species at lower potentials than those observed for pure Pt [7,8]. The atomic Pt:Ru ratio has an important influence on the performance of the catalysts, being the 1:1 the one that gives the highest activity toward CO and methanol oxidation reactions. Therefore, becomes necessary to optimize easy synthesis routes for the preparation of Pt–Ru catalysts, with the desired metal loading and atomic ratio, which develop high electrooxidation activity. With this purpose, different methodologies have been studied using a variety of reducing agents for metal precursors, such as the sodium borohydride [9,10], formic acid [11–16], sodium formate [17], methanol [18] or polyols [19–22].

Regarding the carbon support, in the last few years, the use of novel synthetic carbon supports has attracted much attention. It has been shown that the use of carbon materials with an ordered structure and high electrical conductivity improves the fuel cell performance. These novel non-conventional carbon materials include carbon nanofibers [23,24], carbon nanotubes [25–29], carbon microspheres [30,31], hard carbon spherules [32], carbon

* Corresponding author.
E-mail addresses: epastor@ull.edu.es, elena_pastor_tejera@yahoo.es (E. Pastor).
[1] Dipartimento di Scienze Chimiche, Università di Padova, Via Marzolo 1, 35121 Padova, Italy.

http://dx.doi.org/10.1016/j.apcatb.2014.10.077
0926-3373/© 2014 Elsevier B.V. All rights reserved.

aerogels and xerogels [33,34] and mesoporous carbons [35,36]. Among these, carbon nanofibers (CNFs) have shown to be an excellent carbon support for their suitable textural properties and their high electrical conductivity.

In this work, four different Pt–Ru catalysts supported on CNFs were prepared by the solution-reduction method, using different reducing agents, and their activity toward the CO and methanol electrooxidation reactions were studied. In order to determine the physicochemical properties (e.g. composition, structure and particle size), Pt–Ru/CNF catalysts were characterized by energy-dispersive X-ray (EDX), X-ray diffraction (XRD), X-ray photoelectron spectroscopy (XPS) and transmission electron microscopy (TEM). The electrochemical activities toward CO and methanol oxidation were established by cyclic voltammetry and chronoamperometry techniques, thus the different nanostructures effects toward both reactions can be discerned. In addition, the onset potential for the electrooxidation reactions as well as the energy conversion efficiency of methanol to CO_2 were determined by differential electrochemical mass spectrometry (DEMS).

2. Experimental

2.1. Preparation of carbon support

Carbon nanofibers (CNFs) were synthesized by the catalytic thermal decomposition of methane [37]. Briefly, the CNFs were grown by decomposition of a methane flow on a Ni:Cu:Al catalyst (atomic ratio = 78:6:16) at 700 °C for 10 h [38]. Subsequently, the CNFs were treated in a HNO_3:H_2SO_4 1:1 (v/v) mixture for 0.5 h at room temperature to create surface oxygenated groups (mainly carboxylic, anhydride, phenol and quinones groups [39]) and remove the metals (Ni, Al and Cu). The oxidation conditions were selected from a previous study [39].

2.2. Preparation of carbon-supported Pt–Ru catalysts

Pt–Ru catalysts supported on carbon nanofibers were synthesized by three different methods described below. In all the cases, an appropriate concentration of the precursor salts (H_2PtCl_6, 8%, w/w, solution, Aldrich; and $RuCl_3$, 99.999%, Aldrich) was used to obtain a metal loading of 20 wt% and a Pt:Ru atomic ratio of 1:1.

2.2.1. Sodium borohydride reduction method (BM)

Carbon nanofibers were dispersed in ultrapure water, first under sonication and then under magnetic stirring. Next, the solution containing the metallic precursors was slowly added to the support suspension. In order to promote an homogeneous metal deposition and anchoring, the pH of the suspension was adjusted to 5.0 by concentrated NaOH (98%, Panreac) solution. Subsequently, a 26.4 mM sodium borohydride (99%, Aldrich) solution was added drop by drop under sonication. After 12 h, the mixture was filtered, washed with ultrapure water and dried at 60 °C during 2 h. This catalyst was labeled as Pt–Ru/CNF-BM.

2.2.2. Formate ions reduction method (SFM)

2.0 M HCOOH solution (98–100%, Merck) was adjusted to pH 12.0, and consequently sodium formate ion was produced. The last is necessary to enhance the Ru reduction reaction [17]. After that, carbon nanofibers were dispersed in the sodium formate solution under sonication. Then, the mixture was heated at 80 °C and the solution containing the metallic precursors was slowly added under stirring. The suspension was left under stirring overnight and then was filtered, washed with ultrapure water and dried at 60 °C for 2 h. This catalyst was labeled as Pt–Ru/CNF-SFM.

A portion of this sample was heat-treated at 350 °C in 21% O_2/N_2 atmosphere for 30 min. This sample was labeled as Pt–Ru/CNF-SFM TT.

2.2.3. Methanol reduction method (MeOH)

CNFs were dispersed in a methanol/water (1:3, v/v) mixture under sonication and then 12.5 mg of the surfactant SB-12 was added. Surfactant SB-12 prevents the agglomeration of metal colloids during the reduction stage of metal precursors [18]. Subsequently, the resulting suspension was stirred and refluxed under at 90 °C, and the metal precursors solution (in 1:3, v/v, methanol/water solution) was added drop by drop. The mixture was kept at 90 °C for 1 h and then filtered and washed with ultrapure water. This catalyst was labeled as Pt–Ru/CNF-MeOH.

2.3. EDX, XRD, XPS and TEM characterization

Energy-dispersive X-ray (EDX) analysis carried out by a scanning electron microscope (LEO Mod. 440) at 20 keV, with a Si detector and a Be window, was used to determine the metal content and Pt–Ru atomic ratios of the synthesized catalysts.

X-ray diffraction (XRD) patterns were obtained using a universal diffractometer Panalytical X'Pert operating with Cu Kα radiation generated at 40 kV and 30 mA. Scans were collected at 3° min^{-1} for 2θ values between 20° and 100°. The Scherrer's equation was used to calculate the metal crystallite size using the (220) peak around 2θ = 70°. The lattice parameters were obtained using the (111), (200), (220) and (311) peaks and applying the Vegard's Law.

X-Ray photoelectron spectroscopy (XPS) measurements were performed using a Escalab 250 spectrometer equipped with a concentric hemispherical analyzer, five channeltron detectors and an Al monochromated X-ray source (Kα = 1486.6 eV) operating at 12 kV and 10 mA. The XPS spectra were collected under pressures below 8×10^{-9} mbar. Data processing was performed with the XPSPEAK 4.1® software, after fitting the experimental data with Gaussian–Lorentzian curves, to determine the chemical states of Pt and Ru and the surface composition of the Pt–Ru nanoparticles [40].

TEM analyses were carried out using a transmission electron microscope (200 kV JEOL JEM 2100). An ethanol suspension aliquot of the catalysts was dropped on a carbon grid. MultiScan CCD (794, Gatan) camera was used to obtain the images, which were treated with the Fourier Transform software Digital Micrograh (3.7.0, Gatan).

2.4. Carbon monoxide and methanol electrochemical characterization

An electrochemical water thermostated cell with three electrodes was used for the electrochemical characterization. A glassy carbon disk modified with the different catalysts was used as working electrode, and a glassy carbon bar as counter electrode. A reversible hydrogen electrode (RHE) placed inside a Luggin capillary was used as reference electrode. All potentials are referred to this electrode in the text. For preparing the working electrode, a catalyst ink was prepared using 2 mg of catalyst, 15 μL of Nafion® (5 wt%, Aldrich) and 500 μL of ultra-pure water, subsequently a 40 μL aliquot was deposited on the glassy carbon disk. 0.5 M H_2SO_4 (95–97%, Merck) was used as support electrolyte. Potentiostatic measurements were carried out using a μAUTOLAB III modular equipment. High resistivity deoxygenated 18.2 MΩ H_2O was used for preparing all the solutions. For the CO-stripping measurements, CO (99.999%, Air Liquide) was bubbled into the electrochemical cell for 10 min at 0.2 V *vs.* RHE and 20 °C, in order to form a CO monolayer on the deposited catalyst. Then, nitrogen (MicroGeN_2, GasLab) was bubbled for 10 min to remove the CO from the

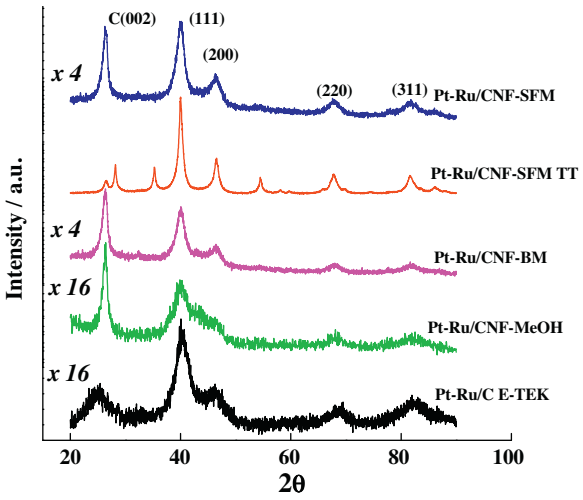

Fig. 1. XRD diffractograms for the Pt–Ru/CNF and the commercial Pt–Ru/C (E-TEK) catalysts.

electrolyte and two potential scans at 20 mV s^{-1}, between 0.050 and 0.85 V were applied. For the methanol (98%, Merck) experiments, 2.0 M solutions were used in these experiments, employing the same potential range, scan rate and temperature.

2.5. DEMS characterization

Differential electrochemical mass spectrometry (DEMS) was employed in order to detect volatile and gaseous products from the electrooxidation of methanol and therefore to achieve the energy conversion efficiency, in addition to check the CO tolerance of the catalysts. Different DEMS designs have been reported in the literature [41,42]. The DEMS cell used in this work has already been described in previous papers [43,44]. It was directly attached to the vacuum chamber of the mass spectrometer (PFEIFFER VACUUM QMS 200) with a Faraday cup detector. The working electrode consisted of a gas diffusion electrode (GDE) with the catalyst deposited onto one side. A RHE and a glassy carbon bar were used as reference and counter electrodes, respectively.

In order to determine the efficiency of the methanol conversion to CO_2, it is necessary to calculate the $m/z = 44$ calibration constant (k^{CO2}). The method for determining k^{CO2} has already been detailed in [44]. This calibration process was carried out before each experiment. This constant was employed for determine the CO_2 conversion percentage, employing Eq. (1):

$$R^{CO_2} = \frac{6 \times Q_i^{CO_2}}{k^{CO_2} \times Q_f^{T}} \quad (1)$$

with Q_f^T being the faradaic charge produced in the methanol oxidation and $Q_i^{CO_2}$ as the ionic charge.

3. Results and discussion

3.1. Physical characterization of the catalysts

Metal content and Pt:Ru atomic ratio were determined by EDX analysis and results are reported in Table 1. All catalysts had similar metal content and Pt:Ru atomic ratio, which were comparable to those of the commercial Pt–Ru/C catalyst from E-TEK. These values were close to the nominal ones, as observed in Table 1.

XRD patterns of the synthesized catalysts are given in Fig. 1. All of them showed the characteristic (111), (200), (220) and (311) peaks of the Pt face centered cubic (fcc) structure. Moreover, in all diffractograms a peak appeared around 24.5° for Pt–Ru/C E-TEK and 26.5° for PtRu/CNF. This feature corresponds to the (002) reflection of graphite basal planes and is attributed to the catalyst support. Additional peaks were observed for the Pt–Ru/CNF-SFM TT sample at 28.5°, 35° and 54°, which may be attributed to crystalline Ru oxides [45] or crystalline phases from Pt and/or Ru segregation [46]. The formation of amorphous Ru-hydrated oxides cannot be excluded, since they are not detectable by XRD [45].

The average crystallite size for the different catalysts was calculated from the (220) reflection by the Debye–Scherrer equation. From these values, the metal surface area (SA) was determined by the equation SA ($m^2\,g^{-1}$) = $6 \times 10^3/\rho d$, where d is the average crystallite size (nm) and ρ is the alloy density. For the ρ calculation, it was considered that ρ_{Pt-Ru} ($g\,cm^{-3}$) = $\rho_{Pt}X_{Pt} + \rho_{Ru}X_{Ru}$, with $\rho_{Pt} = 21.4\,g\,cm^{-3}$ and $\rho_{Ru} = 12.3\,g\,cm^{-3}$, and X_{Pt} and X_{Ru} were the weight percentage of Pt and Ru, respectively. Both the average crystallite size and the metal surface area are reported in Table 1. Pt–Ru/CNF-BM and Pt–Ru/CNF-SFM samples had an average crystallite size of 4.0 and 4.8 nm, respectively. These values were very similar to that for the commercial catalyst (4.4 nm). However, Pt–Ru/CNF-MeOH showed a smaller crystallite size (2.9 nm), which could be justify by the use of the surfactant SB-12 during the synthesis. The heat treatment of the sample prepared by the SFM method led to the sintering of the nanoparticles, since this sample presented an average size of 7.0 nm, whereas before the heat treatment the size was 4.8 nm. This result might be related with desorption of surface oxygenated groups occurred during the heating treatment (it has been reported that surface carboxylic acid groups on the catalyst support are not stable at temperatures higher than 300 °C [39]), inducing the increase of metal nanoparticles size.

The lattice parameters were determined from the X-ray diffractograms and the values are given in Table 1. The lattice parameter for all the Pt–Ru catalysts was lower than that expected for Pt (3.92 Å), indicating the incorporation of the Ru atoms in the Pt fcc structure and, therefore, the formation of Pt–Ru alloy. The atomic radius of Ru is smaller than that for Pt, and accordingly, a contraction of the lattice parameter was expected in the alloy. All values were very similar, as derived from Vegard's law, due to the similar compositions and particle sizes of the catalysts.

The TEM images obtained for the PtRu/CNF catalysts are depicted in Fig. 2. A good dispersion of metal nanoparticles on the support was obtained with the BM, SFM and MeOH synthesis procedures. However, some agglomerates were observed, which is in agreement with results reported in the literature for these synthesis methods [9,47]. The particle size distribution was determined from TEM images (Fig. 2) and, in all cases, as commonly observed for carbon-supported catalysts, the mean particle values obtained from TEM are slightly smaller than crystallite sizes from XRD data (see Table 1).

In order to identify the chemical and electronic states of both metals, as well as the surface composition, XPS analysis was carried out. Table 2 summarizes the results obtained from the XPS study. From the deconvolution of the binding energy spectra of Pt 4f (Fig. 3), three pairs of Pt peaks were found. The peaks close to 71 and 75 eV are attributed to the transitions generated in the $4f_{7/2}$ and $4f_{5/2}$ orbitals for the Pt(0), whereas the second and third pair of peaks, observed at 72–76 and 74.5–77 eV, corresponds to Pt(II) and Pt(IV), respectively [48–52]. For all the materials, Pt(0) was the predominant oxidation state, although a significant amount of oxidized species, mainly Pt(II), was also observed. The presence of Pt oxides on the surface is justified, in part, by the catalyst exposure to the atmosphere. However, clear differences were observed in the relative abundance of Pt(0), Pt(II) and Pt(IV) for the materials prepared with the different synthesis routes. Thus, Pt–Ru/CNF-MeOH displayed the highest Pt(0) relative abundance (75%), which indicates a strong reducing ability of methanol towards this metal,

Table 1
Composition, crystallite size and lattice parameters for Pt–Ru catalysts.

Catalyst	Atomic ratio Pt:Ru	Metal content (wt%)	Crystallite or particle size (nm)		Lattice parameter (Å)	Metal surface area ($m^2 g^{-1}$)
			XRD	TEM		
Pt–Ru/CNF-SFM	48:52	20	4.8	3.3 ± 0.8	3.901	69
Pt–Ru/CNF-SFM TT	46:54	21	7.0	–	3.916	52
Pt–Ru/CNF-BM	47:53	24	4.0	3.0 ± 1.0	3.901	83
Pt–Ru/CNF-MeOH	61:39	18	2.9	3.1 ± 0.7	3.893	112
Pt–Ru/C E-TEK	45:55	20	4.4	–	3.898	76

whereas Ru(0) content was the lowest (see later). Pt–Ru/CNF-BM displayed similar Pt(II) and Pt(IV) contents (34–38 and 7–13%, respectively), than both catalysts produced by formate ions reduction. The commercial catalyst Pt–Ru/C E-TEK exhibited a Pt(0) abundance close to 62% and the lowest contribution in Pt(IV), being the latter comparable with that observed for Pt–Ru/CNF-SFM. Finally, it is remarkable that the Pt–Ru catalyst prepared by the SFM route increased its relative abundance for Pt(IV) from 7 to 13% after the thermal treatment at 350 °C, with a parallel decrease in the contribution of both Pt(0) and Pt(II), deriving in the possible formation of PtO_2 [49]. The fact that these oxides did not appear in the XRD curves can be explained assuming their amorphous and/or surface nature of the oxide in the catalyst.

XPS related to Ru signals are displayed in Fig. 4. The transitions considered are associated to the 3p orbitals in the 450–490 eV binding energy region. For this metal, all catalysts exhibited a doublet

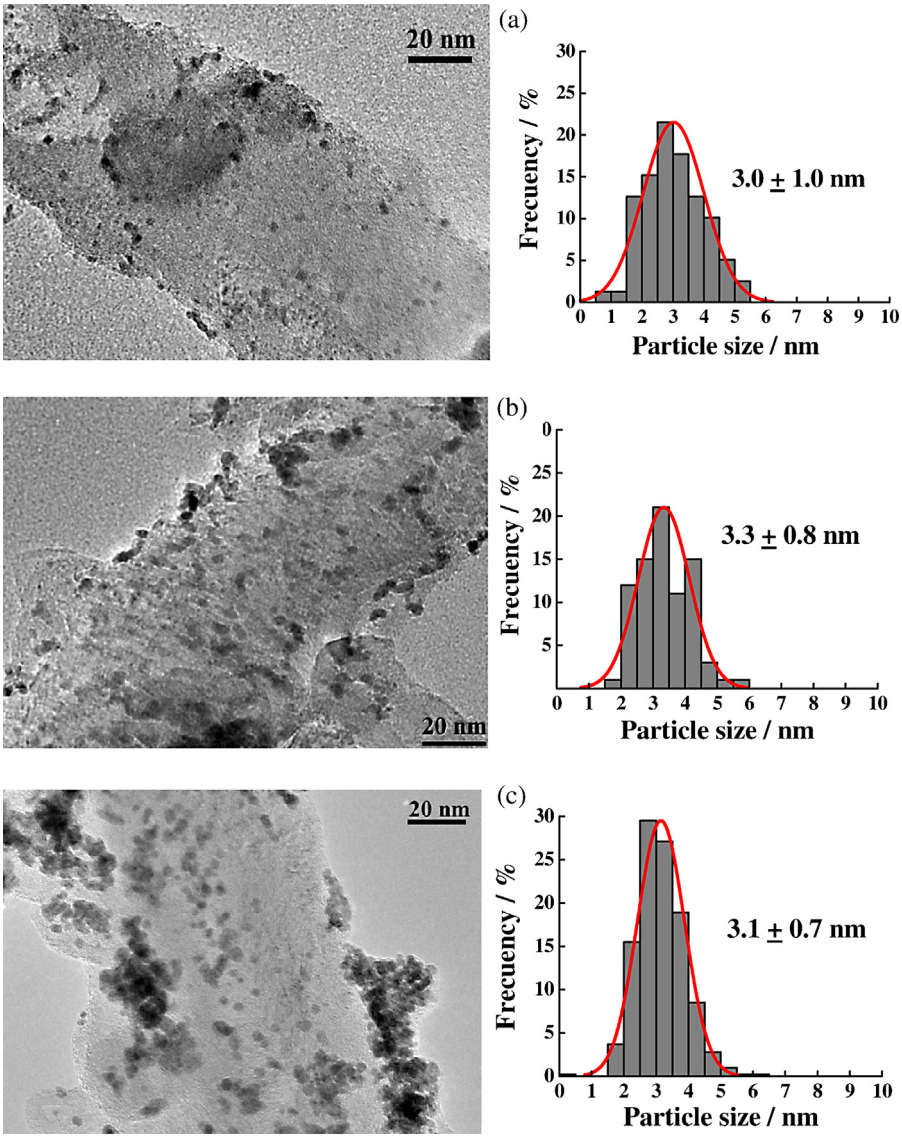

Fig. 2. TEM micrographs (left) and histograms of particle size distribution (right) for the Pt–Ru/CNF-BM (a), Pt–Ru/CNF-SFM (b) and Pt–Ru/CNF-MeOH (c) catalysts.

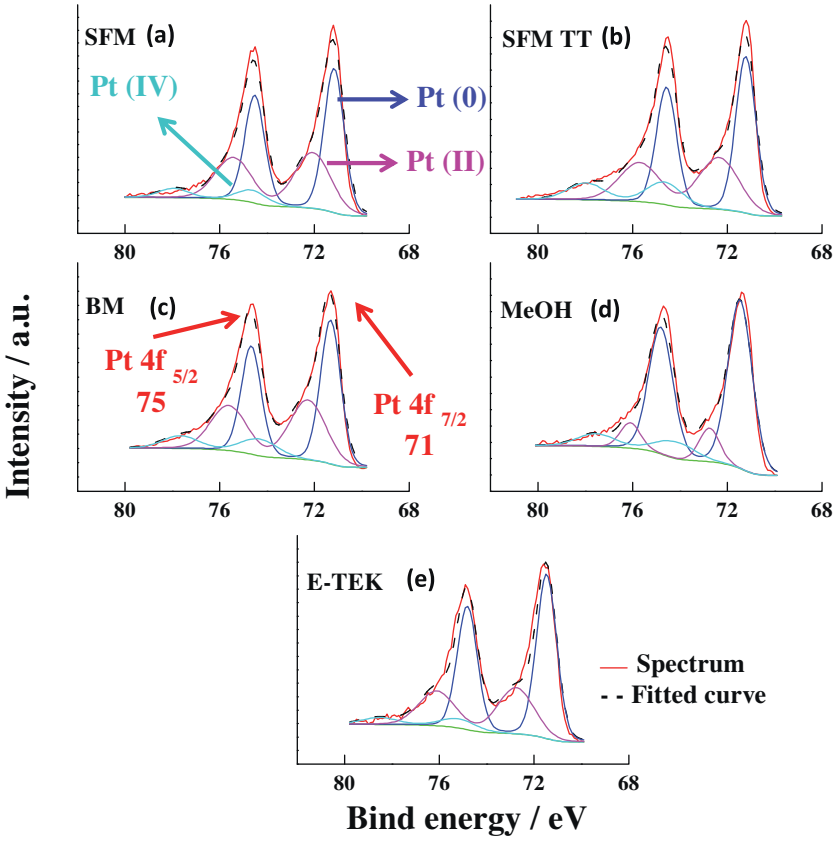

Fig. 3. Pt 4f XPS spectra for the Pt–Ru/CNF-SFM (a), Pt–Ru/CNF-SFM TT (b), Pt–Ru/CNF-BM (c), Pt–Ru/CNF-MeOH (d) and the commercial Pt–Ru/C (E-TEK) (e) catalysts. Blue line: Pt (0). Pink line: Pt (+2). Cyan line: Pt (+4).

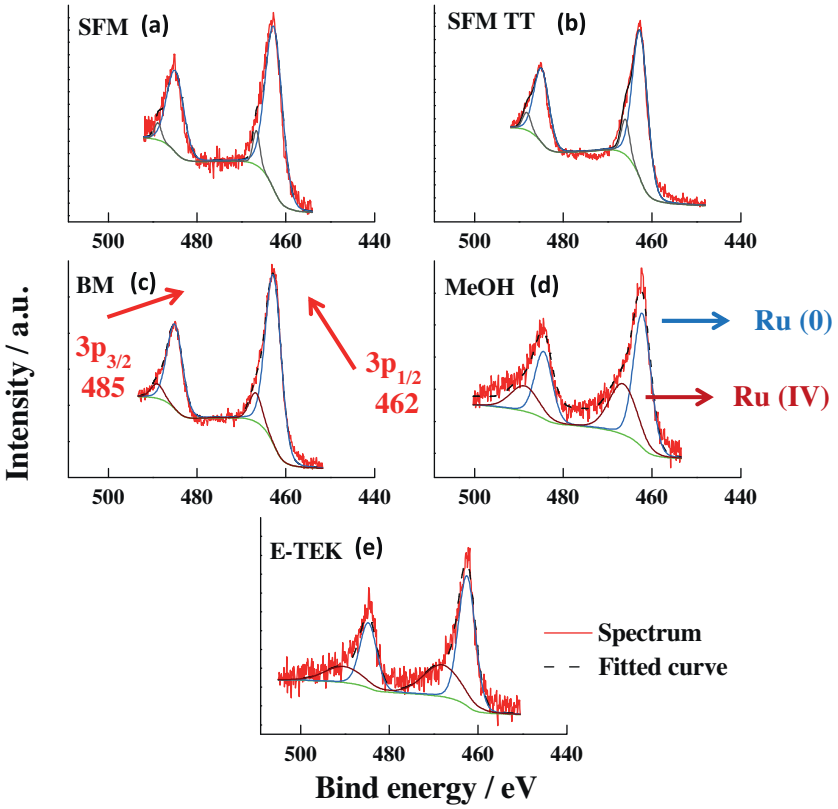

Fig. 4. Ru 3p XPS spectra for the Pt–Ru/CNF-SFM (a), Pt–Ru/CNF-SFM TT (b), Pt–Ru/CNF-BM (c), Pt–Ru/CNF-MeOH (d) and the commercial Pt–Ru/C (E-TEK) (e) catalysts. Light blue line: Ru (0). Brown line: Ru (+4).

Table 2
Electronic and composition parameters of the Pt–Ru/CNF and the commercial Pt–Ru/C E-TEK catalysts obtained from the XPS data.

Catalyst	Pt			Ru		
	Binding energy (eV)	Relative abundance (%)	Assignment	Binding energy (eV)	Relative abundance (%)	Assignment
Pt–Ru/CNF-SFM 61:39*	71.2	55	Pt(0)	462.7	92	Ru(0)
	72.1	38	Pt(II)	466.6	8	Ru(IV)
	74.6	7	Pt(IV)			
Pt–Ru/CNF-SFM TT 58:42*	71.2	52	Pt(0)	462.7	88	Ru(0)
	72.4	34	Pt(II)	466.0	12	Ru(IV)
	74.6	13	Pt(IV)			
Pt–Ru/CNF-BM 46:54*	71.3	51	Pt(0)	462.8	88	Ru(0)
	72.9	38	Pt(II)	466.8	12	Ru(IV)
	74.3	11	Pt(IV)			
Pt–Ru/CNF-MeOH 54:46*	71.5	75	Pt(0)	462.2	59	Ru(0)
	72.8	13	Pt(II)	466.5	41	Ru(IV)
	74.2	12	Pt(IV)			
Pt–Ru/C E-TEK 50:50*	71.5	62	Pt(0)	462.5	65	Ru(0)
	72.8	31	Pt(II)	468.0	35	Ru(IV)
	75.2	6	Pt(IV)			

* Indicates the Pt:Ru atomic ratio on the surface determined from XPS analysis.

attributed to $3p_{1/2}$ and $3p_{3/2}$ transitions from Ru(0) [48] around 462 and 485 eV, respectively, and a second doublet close to 467 and 489 eV indicating the presence of Ru (IV). These transitions were chosen for Ru analysis instead of those close to 280–284 eV [48] because of the presence of the high intensity C 1s signal in the last region, which superimposes the Ru feature [52,53]. For all the catalysts, the predominant oxidation state for Ru was Ru(0) with a relative abundance of 88–92%, with the exception of the commercial material and the sample prepared by the MeOH method, which showed a significant amount of Ru(IV), around 40%, attributed to hydrated amorphous RuO_2 [53]. This value is in agreement with data already reported in the literature [51,53]. As in the case of Pt, no signals corresponding to Ru oxides were apparent in the XRD spectra with the exception of the Pt–Ru/CNF-SFM TT. It was observed that after the heat treatment, some additional peaks were developed in the diffractogram together with an enhancement of the relative abundance of Ru(IV) from 8 to 12% in the XPS signals. This fact could be explained considering the formation of crystalline phases of Ru oxides while increasing the temperature.

Table 2 also shows the Pt:Ru atomic ratios estimated from XPS analysis, which deliver surface composition instead of bulk composition (EDX). Pt–Ru/CNF-BM and commercial Pt–Ru/C E-TEK samples presented the same bulk and surface composition. However, Pt–Ru/CNF-SFM and Pt–Ru/CNF-SFM TT materials suffered a Pt enrichment on the surface since the Pt:Ru ratio increases from 46:54 to 58:42 for Pt–Ru/CNF-SFM TT and from 48:52 to 61:39 for Pt–Ru/CNF-SFM. This result was in good agreement with the higher amount of Pt(II) species in these samples, indicating that Pt is oxidized due to the contact with the atmosphere. Pt–Ru/CNF-MeOH presented the opposite behavior, the Pt surface content (Pt:Ru = 54:46) is lower than in the bulk (Pt:Ru = 61:39). In this case, the surface Ru enrichment by its segregation and subsequent formation of Ru oxides explained the higher amount of Pt(0) in this sample, i.e. Pt was mainly in the core of the nanoparticles and was protected from the atmosphere by the RuO_2 layer formed on the surface.

Summarizing, it is possible to propose certain selectivity toward the oxides formation of Pt or Ru depending on the different synthetic methods utilized. Table 2 shows that a high content of Ru(0) promotes the formation of Pt oxides, as in the case of the materials synthesized with formate ions, verifying the strategy suggested by [17], which mainly consists in the rise of the pH of the formic acid solution in order to guarantee the total reduction of Ru. On the other hand, catalysts with high Pt(0) content exhibited the highest Ru(IV) abundances. So methanol behaves as a strong reducing agent towards Pt but weak for Ru.

3.2. Electrochemical characterization

CO stripping voltammetry was carried out in order to establish the CO tolerance of the Pt–Ru catalysts. After adsorption of CO at 0.2 V, a potential scan up to 0.85 V was performed, oxidizing the CO_{ad} monolayer and developing in this way an anodic wave. The area under the CO oxidation peak was also used to determine the electroactive area, assuming a charge of 420 $\mu C\,cm^{-2}$ involved in the oxidation of a monolayer of linearly adsorbed CO. Current densities given in the present paper were calculated with this electroactive area.

Results obtained for commercial Pt/C and Pt–Ru/C catalysts (E-TEK) are presented in the supporting information (Fig. 1SI), showing the common behavior described in the literature for these materials [54]. The enhanced CO tolerance by Ru insertion is regularly attributed to the bifunctional mechanism [7,8].

Fig. 5 displays the voltammograms for CO_{ad} electrooxidation at the Pt–Ru/CNF catalysts synthesized in this work recorded at 20 mV/s. These curves showed higher tolerance to CO for Pt–Ru/CNF than the commercial Pt–Ru/C catalyst. Thus, both the peak and onset potentials for CO_{ad} oxidation were shift to more negative potentials for the materials supported on CNF. It is remarkable that in the case of Pt–Ru/CNF-SFM TT, two clearly defined oxidation peaks were observed. The pre-peak was already described in [55] for the CO oxidation on Pt–Ru supported on carbon black and thermally treated at 200 °C in a H_2/Ar atmosphere during 1 h. The authors explained this behavior by the enrichment of Pt on the catalyst surface and the presence of Ru oxides, which are able to promote the CO oxidation reaction. So, the same argument can be used to justify the results in the present work, as the formation of Ru oxides after the heat treatment was established from XRD and XPS analysis (Fig. 1 and Table 2). Actually, this heat-treated catalyst exhibited the most negative onset potential for CO oxidation (0.376 V), whereas the first oxidation peak potential was located at 0.478 V. In fact, the catalysts sequence in terms of the onset potential for the CO oxidation reaction is the following:

Pt–Ru/CNF-SFMTT(0.376 V) < Pt–Ru/CNF-MeOH(0.413 V)
< Pt–Ru/CNF-SFM(0.428 V) < Pt–Ru/CE-TEK(0.441 V)
< Pt–Ru/CNF-BM(0.453 V)

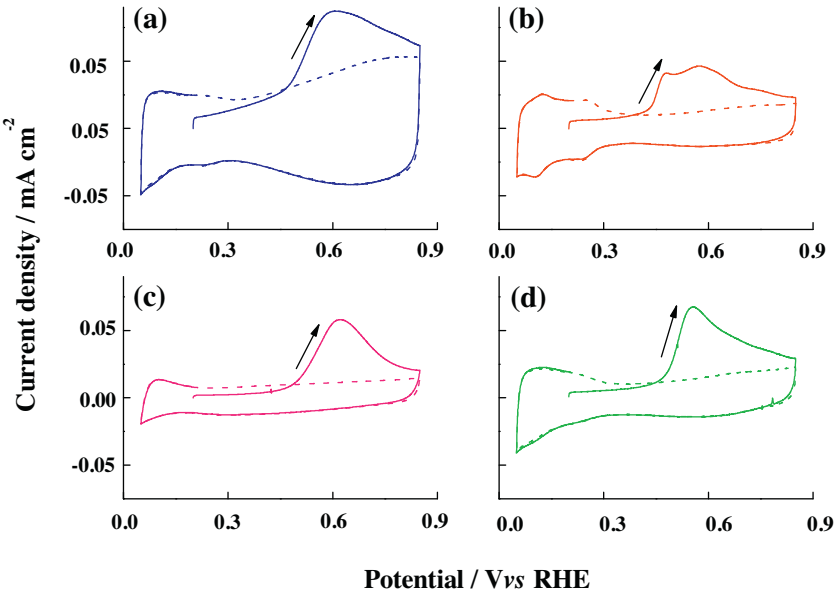

Fig. 5. Cyclic voltammograms for the CO_{ad} oxidation at 20 °C on the Pt–Ru/CNF-SFM (a), Pt–Ru/CNF-SFM TT (b), Pt–Ru/CNF-BM (c) and Pt–Ru/CNF-MeOH (d) catalysts. Solid line: first scan. Dashed line: second scan. Scan rate: 20 mV s^{-1}. Support electrolyte: 0.5 M H_2SO_4. CO adsorption potential: 0.2 V *vs* RHE.

This trend partially matches with that for the CO oxidation peak potential:

Pt–Ru/CNF-SFMTT(fistpeak) < Pt–Ru/CNF-MeOH < Pt–Ru/CE-TEK < Pt–Ru/CNF-SFM < Pt–Ru/CNF-BM

The CO peak position varies between 0.478 and 0.622 V, Pt–Ru/CNF-SFM and Pt–Ru/C E-TEK shift their order, but the general trend is maintained. In this sense, the determination of the onset potential implies a higher error than the peak potential and this fact could be the cause of the differences observed. As will be shown later (Section 3.3), DEMS allows an accurate determination of the onset potential for the CO oxidation reaction. According to these data, Pt–Ru/CNF-SFM TT sample presented the highest CO tolerance. Differences observed during the CO stripping voltammograms for the Pt–Ru/CNF materials could be associated to the surface mobility of adsorbed CO on different crystalline faces [56]. In this context, the synthesis procedure may influence the amount and distribution of these crystalline faces in each catalyst. Another important factor is the composition of the surface, i.e. Pt:Ru ratio, oxides and the oxidation state of the species.

The second scan depicted in Fig. 5 corresponds to the cyclic voltammogram (CV) of a clean Pt–Ru surface, as CO_{ad} was completely oxidized during the first anodic sweep. With the exception of Pt–Ru/CNF-SFM and Pt–Ru/CNF-SFM TT, all the curves developed similar features. Pt–Ru/CNF-SFM TT exhibited higher definition of the hydrogen adsorption/desorption peaks (Fig. 5b), while Pt–Ru/CNF-SFM showed higher anodic currents at $E > 0.60$ V (Fig. 5a). The current response in the hydrogen adsorption/desorption region was in good agreement with the nanoparticle structure deduced from the XPS data, in which a Pt surface enrichment by the thermal treatment was observed for this material. The current densities at $E > 0.60$ V at Pt–Ru/CNF-SFM did not decrease during potential cycling and can therefore be attributed to the presence of synthesis residues from formate ions, strongly adsorbed on Pt sites that were not completely oxidized in the potential range applied. This fact motivated us to carry out a heat treatment at 350 °C in order to remove the organic substances, as can be observed in the Fig. 5b.

Pt–Ru/CNF catalysts were also tested for the electrochemical oxidation of methanol at 20 °C. Cyclic voltammograms shown in Fig. 6 displayed comparable behaviors for all the synthesized catalysts. During the positive-going scan, the onset potential for methanol oxidation was observed between 0.40 and 0.50 V and an irreversible anodic wave is observed at more positive potentials. Pt–Ru/CNF-SFM TT and Pt–Ru/CNF-MeOH materials did not resolve an oxidation peak, since their definition appears at more positive potentials than the potential limit reached in the present conditions. The negative potentials scan showed that the anodic current continues but with lower current densities than the forward scan. In addition, it can be observed a current hysteresis at $E < 0.60$ V, from which the current densities slightly exceed those from the forward scan. Although the shape of the CVs was similar, the current densities depended on the synthesis method. Catalysts synthesized using an organic molecule (formate ions and methanol) as reducing agent exhibited higher current densities, in comparison with that prepared with sodium borohydride. Accordingly, reactivity order (in terms of the maximum current densities) towards 2.0 M methanol

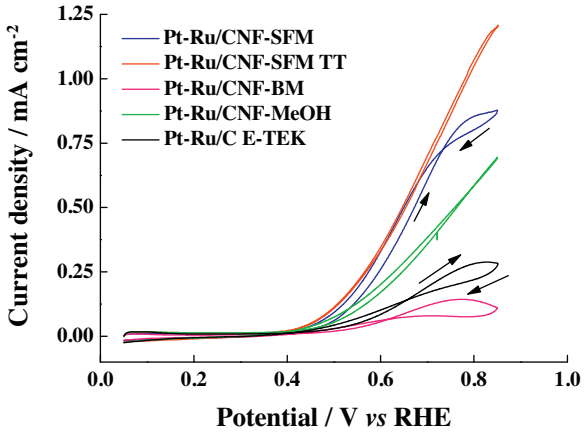

Fig. 6. Cyclic voltammograms for the methanol oxidation at 20 °C on the Pt–Ru/CNF catalysts. Scan rate: 20 mV s^{-1}. Support electrolyte: 0.5 M H_2SO_4. Methanol concentration: 2.0 M.

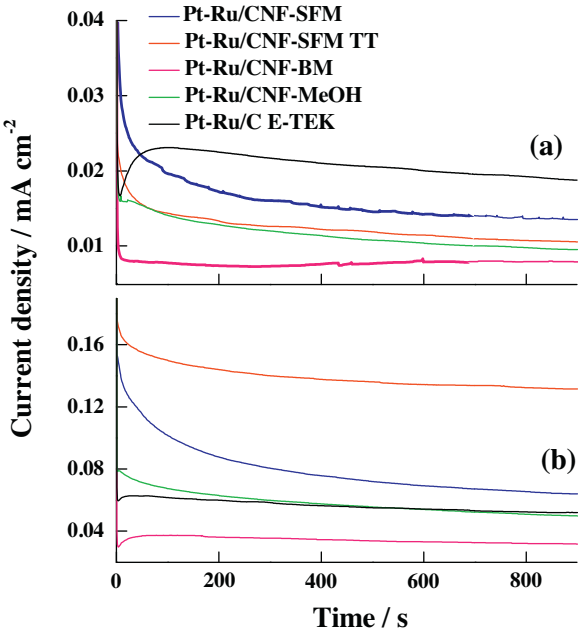

Fig. 7. Current density versus time curves at 20 °C for the methanol oxidation on the Pt–Ru/CNF catalysts. Supporting electrolyte: 0.5 M H_2SO_4. Methanol concentration: 2.0 M. Applied potentials: (a) 0.45 and (b) 0.55 V *vs* RHE.

solution oxidation at 20 °C was:

Pt–Ru/CNF-SFMTT > Pt–Ru/CNF-SFM > Pt–Ru/CNF-MeOH > Pt–Ru/CE-TEK > Pt–Ru/CNF-BM

The Pt–Ru/CNF-SFM TT catalyst displayed the highest current density in Fig. 6. It was almost fivefold higher than the developed by the commercial Pt–Ru/C E-TEK catalyst. Probably the crystalline Ru oxides formed during the thermal treatment of the first catalyst were responsible for the enhancement in the catalytic activity toward the methanol oxidation reaction. It is well known that CO is produced as intermediate in the methanol oxidation process (see later, Eq. (4)), which strongly adsorbs on Pt sites [57,58]. Therefore, the good performance toward methanol oxidation observed for this material could be attributed to the fact that Pt–Ru/CNF-SFM TT oxidizes CO_{ad} at much lower potentials than the other catalysts, and in this way the turnover rate of methanol could be enhanced.

However, these catalytic activities are referred to high overpotentials, i.e. close to 0.85 V. In this sense, these potentials are much higher than those observed under operational conditions in a DMFC. A better correlation between half-cell and DMFC can be achieved by chronoamperometric experiments, in which the methanol oxidation current densities can be registered in the steady state. Current transients recorded at 0.45 (Fig. 7a) and 0.55 V (Fig. 7b) *vs.* RHE at 20 °C in methanol solution are depicted in Fig. 7. High catalytic activity toward methanol oxidation was observed at the lower applied potential for commercial and the catalysts synthesized by the formate ions procedure (Pt–Ru/CNF-SFM and Pt–Ru/CNF-SFM TT). On the other hand, Pt–Ru/CNF-SFM and specially Pt–Ru/CNF-SFM TT catalysts raised their activity at 0.55 V, developing the highest current densities. The activities registered at this potential were in agreement with those results obtained by cyclic voltammetry (Fig. 6).

For the complete analysis of the methanol electrochemical oxidation, it is necessary to consider the proposed mechanism for this reaction [7]:

$$CH_3OH \rightleftharpoons CH_3OH_{ads} \quad (2)$$

$$CH_3OH_{ads} \rightarrow CO_{ad} + 4H^+ + 4e^- \quad (3)$$

$$H_2O \rightarrow OH_{ad} + H^+ + e^- \quad (4)$$

$$CO_{ad} + OH_{ad} \rightarrow CO_2 + H^+ + e^- \quad (5)$$

After adsorption of the alcohol (Eq. (2)), deprotonation of methanol occurs (Eq. (3)) forming CO_{ad} that is oxidized by OH_{ad} (produced from water dissociation in Eq. (4)), generating CO_2 and liberating the catalytic surface (Eq. (5)). Taking into account the results for the CO electrochemical oxidation (Figs. S1 and S5) and considering that this reaction is also involved during the methanol oxidation (Eq. (5)), the catalytic activity for the oxidation of this fuel may follow the same catalyst trend than for the CO_{ad} oxidation in terms of the oxidation potentials. Therefore, high activity toward the CO_{ad} oxidation reaction (high CO tolerance, low onset and peak oxidation potential) facilitates Eq. (5) and may increase the activity toward the alcohol oxidation.

Thus, if CO_{ad} oxidation reaction is favored, then methanol adsorption and dehydrogenation steps (Eqs. (2) and (3)) may become the rate-determining steps. It has to be taken in mind that methanol does not adsorb/react on Ru at 20 °C but promote the water dissociation reaction (Eq. (4)). Then Eqs. (2) and (3) can occur only on Pt atoms. For this reason, Pt surface enrichment (determined by XPS) appears to be another important factor in the methanol oxidation reaction. The following depicts the percentage of Pt in the catalyst surface:

Pt–Ru/CNF-SFM(61%) > Pt–Ru/CNF-SFMTT(58%) > Pt–Ru/CNF-MeOH(54%) > Pt–Ru/CE-TEK(50%) > Pt–Ru/CNF-BM(46%).

Also, the presence of Ru oxides in the catalyst surface and the increment of particle size for Pt–Ru/CNF-SFM TT play an important role in the catalytic activity towards methanol oxidation reaction. Additionally, it is clearly observed some differences in activity between different approaches, i.e. potentiodynamic and potentiostatic measurements. Indeed, the operational voltage is an important factor that controls the overall reaction.

Thus, the main difference between Pt–Ru/CNF-SFM TT and Pt–Ru/CNF-SFM is the higher particle size of the former, which may indicate surfaces (terraces) with higher length and lower density of active sites for water dissociation (low-coordinated sites such as steps and kinks). Therefore, a more suitable surface for methanol adsorption (Eq. (2)) on Pt–Ru/CNF-SFM TT is expected, and an increment of the applied potential from 0.45 to 0.55 V can produce an increase of the kinetic of methanol dehydrogenation (Eq. (3)) and water dissociation reactions (Eq. (4)). In this context, the rise in the applied potential greatly increases the catalytic activity toward methanol oxidation on Pt–Ru/CNF-SFM TT catalyst, and therefore the dehydrogenation step seems to be the main responsible for this effect.

Finally, the presence of different preferential crystallographic planes, formed during the synthesis process, may react in diverse way toward the methanol reaction, considering the well-known dependence of methanol reactivity with some Pt crystalline faces [59]. Nevertheless, from the studies performed in this work, it is not possible to obtain conclusions about the influence of this parameter.

3.3. *DEMS characterization*

DEMS measurements were applied to establish the onset potential for CO and methanol electrooxidation and the current energy conversion efficiency of methanol to CO_2. DEMS allows the simultaneous acquisition of cyclic voltammograms (CVs) and mass

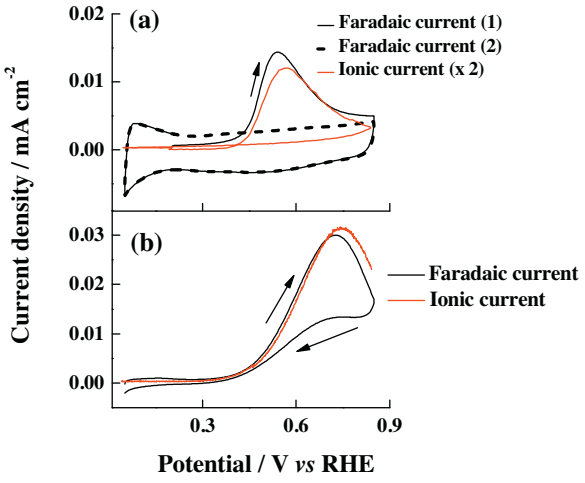

Fig. 8. DEMS characterization for the CO_{ad} (a) and methanol (b) oxidation reactions on the commercial Pt–Ru/C (E-TEK) catalyst. Scan rate: 5 mV s^{-1}. Support electrolyte: 0.5 M H_2SO_4. CO adsorption potential: 0.20 V *vs* RHE. Methanol concentration: 0.5 M.

spectrometric cyclic voltammograms (MSCVs), which are recorded at 5 mV/s.

The experimental faradaic (black lines) and theoretical (red lines) currents of CO stripping (upper panel) and methanol electrooxidation (lower panel) for the commercial Pt–Ru/C E-TEK are depicted in Fig. 8. Theoretical currents are calculated from the ion current of the $m/z = 44$ signal after DEMS system calibration (see Section 2.4). The onset potentials for both reactions were determined from the theoretical curves (red lines), which were obtained multiplying the ion currents of the $m/z = 44$ signal by k^{CO2} (see Section 2.4 for calculations). In this way, the onset potential for the CO stripping at Pt–Ru/C E-TEK sample was established at 0.310 V (red line). A remarkable potential shift of 0.120 V in the onset potential for the CO oxidation reaction was observed between the faradaic and ionic currents, which shows the error involved in the determination from the faradaic currents (see Table 3). On the other hand, similar onset potentials for the methanol electrooxidation were achieved with faradaic and ionic currents. Then, the importance of the use of DEMS to establish the onset potential of processes involving adsorbed monolayers (which implies low current densities) is confirmed. It should be noticed that a scan rate of 5 mV/s was used for DEMS studies (instead of the 20 mV/s employed in Section 3.2).

Table 3
Onset potential for the CO electrooxidation determined from the signal $m/z = 44$ and cyclic voltammetry from DEMS experiments.

Catalyst	Ionic current $m/z = 44$ E_{onset} (V)	CV E_{onset} (V)
Pt–Ru/CNF-BM	0.335	0.380
Pt–Ru/CNF-SFM	0.289	0.389
Pt–Ru/CNF-SFM TT	0.252	0.367
Pt–Ru/CNF-MeOH	0.256	0.444
Pt–Ru/C E-TEK	0.310	0.430

Table 4
Efficiency to CO_2 for methanol electrooxidation calculated by DEMS.

Catalyst	CO_2 conversion efficiency (%)
Pt–Ru/C E-TEK	96
Pt–Ru/CNF-SFM	93
Pt–Ru/CNF-SFM TT	79
Pt–Ru/CNF-BM	89
Pt–Ru/CNF-MeOH	82

CVs and MSCVs ($m/z = 44$) for the CO_{ad} electrochemical oxidation at all synthesized Pt–Ru materials are depicted in Fig. 9, while the onset potentials values for this reaction are reported in Table 3. In all the studied materials, the values acquired from the $m/z = 44$ signal were lower than those observed from the CVs, and follow the subsequent trend:

$$\text{Pt–Ru/CNF-SFMTT} < \text{Pt–Ru/CNF-MeOH} < \text{Pt–Ru/CNF-SFM} < \text{Pt–Ru/CE-TEK} < \text{Pt–Ru/CNF-BM}$$

Energy efficiency conversion of methanol to CO_2 was determined from the CVs and MSCVs depicted in Figs. 8b and 10, applying Eq. (1). The main difference between theoretical and faradaic currents was assigned to by-side products different to CO_2, e.g. formic acid and formaldehyde. Additionally, the difference between faradaic and theoretical currents was utilized to calculate the energy efficiency conversion to CO_2 (Table 4). It is observed that commercial catalyst (Pt–Ru/C E-TEK) developed the highest energy efficiency conversion, which was close to 100%, in agreement with published results [44]. The synthesized catalysts displayed energy efficiency conversion of methanol to CO_2 between 93 and 82% with

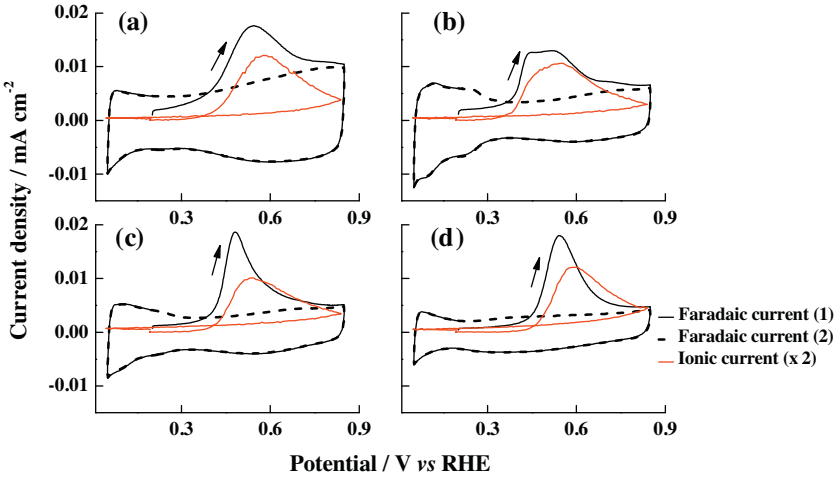

Fig. 9. DEMS characterization for the CO_{ad} oxidation on the catalysts: (a) Pt–Ru/CNF-SFM, (b) Pt–Ru/CNF-SFM TT, (c) Pt–Ru/CNF-BM and (d) Pt–Ru/CNF-MeOH. Scan rate: 5 mV s^{-1}. Support electrolyte: 0.5 M H_2SO_4. CO adsorption potential: 0.20 V *vs* RHE.

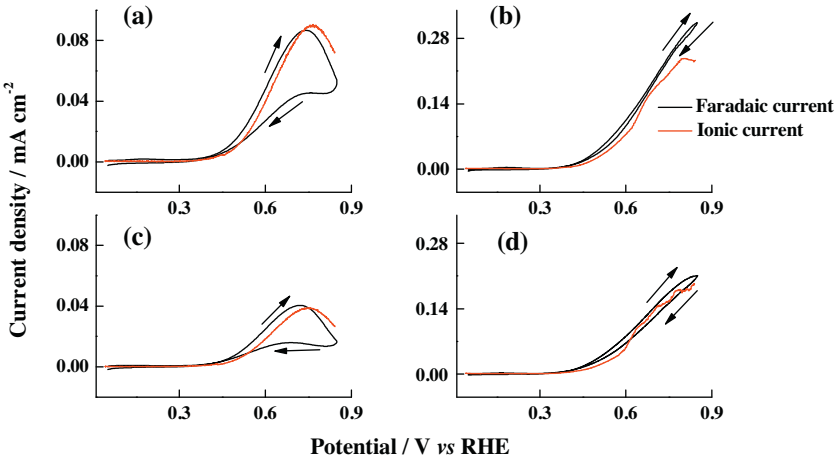

Fig. 10. DEMS characterization for the methanol oxidation on the Pt–Ru/CNF-SFM (a), Pt–Ru/CNF-SFM TT (b), Pt–Ru/CNF-BM (c) and Pt–Ru/CNF-MeOH (d) catalysts. Scan rate: 5 mV s^{-1}. Support electrolyte: 0.5 M H_2SO_4. Methanol concentration: 0.5 M.

the following tendency:

Pt–Ru/CNF-SFM > Pt–Ru/CNF-BM > Pt–Ru/CNF-MeOH > Pt–Ru/CNF-SFMTT

It is remarkable that Pt–Ru/CNF-SFM TT presented the lowest energy conversion efficiency to CO_2 (79%) and the highest current densities during the methanol oxidation reaction. Therefore, these currents must be related with the formation of partially oxidized products, such as formaldehyde and/or formic acid. This result is in agreement with the observed above, in which the high particle size (terraces with high length) of this material determines the reaction path. It seems that long terraces increase the methanol adsorption and dehydrogenation steps, but also the diffusion of soluble intermediates, such as aldehydes and acids, to the bulk solution, and as consequence the turnover rate of methanol increases (higher faradaic currents) and the energy conversion efficiency to CO_2 decreases.

4. Conclusions

Pt–Ru/CNF catalysts with a Pt:Ru atomic ratio of 1:1 were synthesized by the solution-reduction method using different reducing agents such as sodium borohydride, formate ions and methanol (BM, SFM and MeOH methods, respectively). It was observed that the physicochemical properties of the Pt–Ru catalysts depend on the synthesis procedure. Nanoparticle (NP) sizes of ca. 4 nm were obtained by the BM and SFM methods. MeOH procedure produced smaller particle size (3 nm), which may be caused by the use of the SB-12 surfactant during the synthesis. Heat treatment of the sample prepared by the SFM method developed particles close to 7 nm diameter with crystalline Ru oxides. XPS analysis established a Pt surface enrichment for the materials produced by the SFM method, whereas the samples prepared by the MeOH procedure showed a surface rich in RuO_2. The BM method produced Pt–Ru NPs with the same atomic ratio of both metals in the bulk and the surface of the particle, and low amount of (presumably amorphous) Ru oxides in the surface was discerned.

Pt–Ru/CNF catalysts displayed different activities towards the CO and methanol electrooxidation reactions. The sample prepared by the SFM method and subjected to the heat treatment (Pt–Ru/CNF-SFM TT) exhibited the highest tolerance to CO, which can be attributed to the crystalline Ru oxides formed during the thermal treatment. This sample also produced the highest current densities during the methanol electrooxidation, although it showed the lowest energy efficiency conversion of methanol to CO_2. The last result was associated to the higher particle size obtained by this method. Besides the catalysts produced by the BM procedure, synthesized CNF-supported materials exhibited higher CO tolerance and catalytic activity toward the methanol oxidation reaction than the commercial Pt–Ru/C (E-TEK) material. However, the last catalyst was found to be the most efficient in the conversion of methanol to CO_2.

From these studies, it can be concluded that the particle synthesis procedure determines paramount factors for increasing the activity of each desired reaction. Surface composition, chemical states of the specimen, atomic surface structure, catalyst support and particle size (length of surface domains) are some of the main factors that control the catalytic activity.

Acknowledgements

This work was carried out with the help of Project MINECO (MAT2011-28913-C03-01 y-02) of the Spanish Ministry of Science and Technology. J. C. C. is indebted to the Alβan Program for the predoctoral fellowship No. E07D403742CO. The authors want to thank the Electrochemistry, Materials and Environment Laboratory of the University of Barcelona and the Institute of Catalysis and Petrochemistry (CSIC) for the TEM analysis.

Appendix A. Supplementary data

Supplementary data associated with this article can be found, in the online version, at http://dx.doi.org/10.1016/j.apcatb.2014.10.077.

References

[1] E. Antolini, E.R. Gonzalez, Electrochim. Acta 56 (2010) 1–14.
[2] J. Goel, S. Basu, Energ. Procedia 28 (2012) 66–77.
[3] L. Ma, X. Zhao, F. Si, C. Li, J. Liao, L. Liang, W. Xing, J. Power Sources 55 (2010) 9105–9112.
[4] V.V. Kusnetsov, B.I. Podlovchenko, R.I. Shakurov, K.V. Kavyrshina, S.E. Lyahenko, Int. J. Hydrogen Energ. 39 (2014) 829–836.
[5] J.M. Sieben, M.M.E. Duarte, Int. J. Hydrogen Energ. 37 (2012) 9941–9947.
[6] Y. Li, L. Zheng, S. Liao, J. Zeng, J. Power Sources 196 (2011) 10570–10575.
[7] M. Watanabe, S. Motoo, J. Electroanal. Chem. 60 (1975) 267–273.
[8] H.A. Gasteiger, N.M. Markovic, P.N. Ross Jr., J. Phys. Chem. 99 (1995) 8290–8301.
[9] M. Harada, H. Einaga, J. Colloid Interf. Sci. 308 (2007) 568–572.
[10] D. Nagao, Y. Shimazaki, S. Saeki, Y. Kobayashi, M. Konno, Colloid Surf. A 302 (2007) 623–627.

[11] E.R. Gonzalez, E.A. Ticianelli, A.L.N. Pinheiro, J. Perez, Brazilian Patent INPI-SP No. 00321 (1997).
[12] W.H. Lizcano-Valbuena, V.A. Paganin, E.R. Gonzalez, Electrochim. Acta 47 (2002) 3715–3722.
[13] F. Colmati Jr., W.H. Lizcano-Valbuena, G.A. Camara, E.A. Ticianelli, E.R. Gonzalez, J. Braz. Chem. Soc. 13 (2002) 474–482.
[14] A.O. Neto, J. Perez, E.R. Gonzalez, E.A. Ticianelli, J. New Mater. Electrochem. Syst. 2 (1999) 189–195.
[15] J.R.C. Salgado, J.C.S. Fernandes, A.M. Botelho do Rego, A.M. Ferraria, R.G. Duarte, M.G.S. Ferreira, Electrochim. Acta 56 (2011) 8509–8518.
[16] J.R.C. Salgado, V.A. Paganin, E.R. Gonzalez, M.F. Montemor, I. Tacchini, A. Ansón, M.A. Salvador, P. Ferreira, F.M.L. Figueiredo, M.G.S. Ferreira, Int. J. Hydrogen Energ. 38 (2013) 910–920.
[17] L. dos Santos, F. Colmati, E.R. Gonzalez, J. Power Sources 159 (2006) 869–877.
[18] X. Wang, I.M. Hsing, Electrochim. Acta 47 (2002) 2981–2987.
[19] S. Yan, G. Sun, J. Tian, L. Jiang, J. Qi, Q. Xin, Electrochim. Acta 52 (2006) 1692–1696.
[20] Z. Liu, L. Hong, J. Appl. Electrochem. 37 (2007) 505–510.
[21] H. Li, G. Sun, L. Cao, L. Jiang, Q. Xin, Electrochim. Acta 52 (2007) 6622–6629.
[22] P. Kanninen, M. Borghei, V. Ruiz, E.I. Kauppinen, T. Kallio, J. Yi, Int. J. Hydrogen Energ. 37 (2012) 19082–19091.
[23] D. Sebastián, J.C. Calderón, J.A. González-Expósito, E. Pastor, M.V. Martínez-Huerta, I. Suelves, R. Moliner, M.J. Lázaro, Int. J. Hydrogen Energ. 35 (2010) 9934–9942.
[24] D. Sebastián, I. Suelves, E. Pastor, R. Moliner, M.J. Lázaro, Appl. Catal. B Environ. 132–133 (2013) 13–21.
[25] X. Yang, J. Zheng, M. Zhen, X. Meng, F. Jiang, T. Wang, C. Shu, L. Jiang, C. Wang, Appl. Catal. B Environ. 121–122 (2012) 57–64.
[26] X. Jin, B. He, J. Miao, J. Yuan, Q. Zhang, L. Niu, Carbon 50 (2012) 3083–3091.
[27] W. Li, C. Liang, W. Zhou, J. Qiu, Z. Zhou, G. Sun, Q. Xin, J. Phys. Chem. B 107 (2003) 6292–6299.
[28] Y. Cheng, S.P. Jiang, Electrochim. Acta 99 (2013) 124–132.
[29] H. Tang, J.H. Chen, Z.P. Huang, D.Z. Wang, Z.F. Ren, L.H. Nie, Y.F. Kuang, S.Z. Yao, Carbon 42 (2004) 191–197.
[30] Y.C. Liu, X.P. Qiu, Y.Q. Huang, W.T. Zhu, Carbon 40 (2002) 2375–2380.
[31] Y.C. Liu, X.P. Qiu, Y.Q. Huang, W.T. Zhu, J. Power Sources 111 (2002) 160–164.
[32] R. Yang, X. Qiu, H. Zhang, J. Li, W. Zhu, Z. Wang, X. Huang, L. Chen, Carbon 43 (2005) 11–16.
[33] J.C. Calderón, N. Mahata, M.F.R. Pereira, J.L. Figueiredo, V.R. Fernandes, C.M. Rangel, L. Calvillo, M.J. Lázaro, E. Pastor, Int. J. Hydrogen Energ. 37 (2012) 7200–7211.
[34] N. Job, J. Marie, S. Lambert, S. Berthon-Fabry, P. Achard, Energ. Convers. Manage. 49 (2008) 2461–2470.
[35] L. Calvillo, M.J. Lázaro, E.G. Bordejé, R. Moliner, P.L. Cabot, I. Esparbé, E. Pastor, J.J. Quintana, J. Power Sources 169 (2007) 59–64.
[36] M.M. Bruno, M.A. Petruccelli, F.A. Viva, H.R. Corti, Int. J. Hydrogen Energ. 38 (2013) 4116–4123.
[37] I. Suelves, M.J. Lázaro, R. Moliner, B.M. Corbella, J.M. Palacios, Int. J. Hydrogen Energy 30 (2005) 1555–1567.
[38] I. Suelves, M.J. Lázaro, R. Moliner, Y. Echegoyen, J.M. Palacios, Catal. Today 116 (2006) 271–280.
[39] L. Calvillo, M.J. Lázaro, I. Suelves, Y. Echegoyen, E.G. Bordejé, R. Moliner, J. Nanosci. Nanotech. 9 (2009) 4164–4169.
[40] C.D. Wagner, L.E. Davis, M.V. Zeller, J.A. Taylos, R.H. Raymond, L.H. Gale, Surf. Interf. Anal. 3 (1981) 211–225.
[41] H. Baltruschat, J. Am. Soc. Mass Spectrom. 15 (2004) 1693–1706.
[42] H. Wang, L.R. Alden, F.J. DiSalvo, H.D. Abruña, Langmuir 25 (2009) 7725–7735.
[43] G.A. Planes, G. García, E. Pastor, Electrochem. Commun. 9 (2007) 839–844.
[44] S. Pérez-Rodríguez, M. Corengia, G. García, C.F. Zinola, M.J. Lázaro, E. Pastor, Int. J. Hydrogen Energy 37 (2012) 7141–7151.
[45] D.R. Rolison, P.L. Hagans, K.E. Swider, J.W. Long, Langmuir 15 (1999) 774–779.
[46] E.S. Steirgerwalt, G.A. Deluga, D.E. Cliffel, C.M. Lukehart, J. Phys. Chem. B 105 (2001) 8097–8101.
[47] W.H. Lizcano-Valbuena, D.C. de Azevedo, E.R. Gonzalez, Electrochim. Acta 49 (2004) 1289–1295.
[48] C.D. Wagner, W.M. Riggs, L.E. David, J.F. Moulder, G.E. Muilenberg, Handbook of X-ray Photoelectron Spectroscopy, Perkin-Elmer Corporation, Eden Prairle, 1978.
[49] C. Bock, C. Paquet, M. Couillard, G.A. Botton, B.R. MacDougall, J. Am. Chem. Soc. 126 (2004) 8028–8037.
[50] X. Zhang, K. Tsang, K. Chan, J. Electroanal. Chem. 573 (2004) 1–9.
[51] K.S. Lee, S.J. Yoo, J.H. Jang, Y.E. Sung, Electrochim. Acta 56 (2011) 8688–8694.
[52] J.R.C. Salgado, J.C.S. Fernandes, A.M. Botelho do Rego, A.M. Ferraria, R.G. Duarte, M.G.S. Ferreira, Electrochim. Acta 56 (2011) 8509–8518.
[53] X. Yang, J. Zheng, M. Zhen, X. Meng, F. Jiang, T. Wang, C. Shu, L. Jiang, C. Wang, Appl. Catal. B: Environ. 121–122 (2012) 57–64.
[54] H.A. Gasteiger, N.M. Markovic, P.N. Ross Jr., E.J. Cairns, J. Phys. Chem. 98 (1994) 617–625.
[55] T.Y. Jeon, K.S. Lee, S.J. Yoo, Y.H. Cho, S.H. Kang, Y.E. Sung, Langmuir 26 (2010) 9123–9129.
[56] F. Maillard, M. Eikerling, O.V. Cherstiouk, S. Schreier, E. Savinova, U. Stimming, Faraday Discuss. 125 (2004) 357–377.
[57] V.S. Bagotzky, Y.B. Vassiliev, O.A. Khazova, J. Electroanal. Chem. Int. Electrochem. 81 (1977) 229–238.
[58] W. Vielstich, T. Iwasita, R. Dalbeck, Handbook for Heterogeneous Catalysis, VCH, Weinheim, 1996.
[59] X.H. Xia, T. Iwasita, F. Ge, W. Vielstich, Electrochim. Acta 41 (1996) 711–718.